



**HAL**  
open science

## Mass-detection of a matter concentration projected near the cluster Abell 1942: Dark clump or high-redshift cluster?

Th. Erben, L. van Waerbeke, Y. Mellier, P. Schneider, J. -C. Cuillandre, F. J. Castander, M. Dantel-Fort

### ► To cite this version:

Th. Erben, L. van Waerbeke, Y. Mellier, P. Schneider, J. -C. Cuillandre, et al.. Mass-detection of a matter concentration projected near the cluster Abell 1942: Dark clump or high-redshift cluster?. Astronomy and Astrophysics - A&A, 2000, 355, pp.23-36. 10.48550/arXiv.astro-ph/9907134. hal-04110380

**HAL Id: hal-04110380**

**<https://hal.science/hal-04110380v1>**

Submitted on 16 Jun 2023

**HAL** is a multi-disciplinary open access archive for the deposit and dissemination of scientific research documents, whether they are published or not. The documents may come from teaching and research institutions in France or abroad, or from public or private research centers.

L'archive ouverte pluridisciplinaire **HAL**, est destinée au dépôt et à la diffusion de documents scientifiques de niveau recherche, publiés ou non, émanant des établissements d'enseignement et de recherche français ou étrangers, des laboratoires publics ou privés.

# Mass-detection of a matter concentration projected near the cluster Abell 1942: Dark clump or high-redshift cluster?\*

Th. Erben<sup>1</sup>, L. van Waerbeke<sup>2,1</sup>, Y. Mellier<sup>3,6</sup>, P. Schneider<sup>1</sup>, J.-C. Cuillandre<sup>4</sup>, F.J. Castander<sup>5</sup>, and M. Dantel-Fort<sup>6</sup>

<sup>1</sup> Max-Planck-Institut für Astrophysik, P.O. Box 1523, 85740 Garching, Germany

<sup>2</sup> CITA, University of Toronto, 60 St. George Street, Toronto, Ontario, M5S 1A7, Canada

<sup>3</sup> Institut d'Astrophysique de Paris, 98bis Boulevard Arago, 75014 Paris, France

<sup>4</sup> CFHT Corporation, P.O. Box 1597, Kamuela, Hawaii 96743, USA

<sup>5</sup> OMP, 14 Av. Edouard Belin, 31400 Toulouse, France

<sup>6</sup> Observatoire de Paris, DEMIRM, 77 avenue Denfert Rochereau, 75014 Paris, France

Received 15 July 1999 / Accepted 25 November 1999

**Abstract.** A weak-lensing analysis of a wide-field  $V$ -band image centered on the cluster Abell 1942 ( $z = 0.223$ ) has uncovered the presence of a mass concentration projected  $\sim 7$  arcminutes South of the cluster center. From an additional wide-field image, taken with a different camera in the  $I$ -band, the presence of this mass concentration is confirmed. A statistical analysis, using the aperture mass technique, shows that the probability of finding such a mass concentration at the observed position from a random alignment of background galaxies is  $10^{-6}$  and  $4 \times 10^{-4}$  for the  $V$ - and  $I$ -band image, respectively. No obvious strong concentration of bright galaxies is seen at the position of the mass concentration, but a slight galaxy number overdensity is present about  $1'$  away from its center. Archival ROSAT-HRI data show the presence of a weak extended X-ray source near to the mass concentration, but also displaced by about  $1'$  from its center, and very close to the center of the slight galaxy number concentration.

From the spatial dependence of the tangential alignment around the center of the mass concentration, a rough mass estimate can be obtained which depends strongly on the assumed redshift of the lens and the redshift distribution of the galaxies which are used for measuring the lensing signal. A lower bound on the mass inside a sphere of radius  $0.5h^{-1}$  Mpc is  $1 \times 10^{14}h^{-1}M_{\odot}$ , considerably higher than crude mass estimates based on the X-ray data. Shifting the lens to higher redshift increases both the lensing and X-ray mass estimates, but does not resolve the mass discrepancy.

Concerning the nature of the mass concentration, no firm conclusion can be drawn from the available data. If it were a high-redshift cluster, the weak X-ray flux would indicate that it had an untypically low X-ray luminosity for its mass; if the

X-ray emission were physically unrelated to the mass concentration, e.g. coming from the relatively low-redshift group which shows up in the number density of galaxies, this conclusion would be even stronger.

Since the search for massive halos by weak lensing enables us for the first time to select halos based on their mass properties only, it is possible that new types of objects can be detected, e.g. halos with very little X-ray and/or optical luminosity, should they exist. The mass concentration in the field of A1942 may be the first example of such a halo. Possibilities to establish the nature of this mass concentration with future observations are briefly discussed.

**Key words:** galaxies: clusters: general – cosmology: observations – cosmology: dark matter – cosmology: gravitational lensing

## 1. Introduction

The abundance of clusters of galaxies as a function of mass and redshift provides one of the most sensitive cosmological tests (e.g. Richstone et al. 1992). In particular, in a high-density Universe, the abundance of massive clusters strongly decreases with redshift, so that the existence of a few massive high-redshift clusters can in principle rule out an  $\Omega_0 = 1$  model (e.g. Eke et al. 1996; Bahcall & Fan 1998).

The reliability of the test depends on the detection efficiency and selection effects in existing samples of clusters whose understanding may be critical. Currently, clusters are selected either by their optical appearance as overdensities of galaxies projected onto the sky and/or in color-magnitude diagrams, or by their X-ray emission. Both selection techniques may bias the resulting sample towards high-luminosity objects, i.e. they would under-represent clusters with high mass-to-(optical or X-ray) light ratio. Furthermore, the observed properties have to be related to their mass in order to compare the observed abundance to cosmological predictions. The usual procedures

---

Send offprint requests to: (erben@mpa-garching.mpg.de)

\* based on observations with the Canada-France-Hawaii Telescope (CFHT) operated by the National Research Council of Canada (CNRC), the Institut des Sciences de l'Univers (INSU) of the Centre National de la Recherche Scientifique (CNRS) and the University of Hawaii (UH) and on data obtained through the NASA/GSFC HEASARC Online archive.

assume a dynamical and/or hydrostatic equilibrium state as well as the geometry of the mass distribution, which in general may be questionable and fairly poorly justified from a theoretical point of view.

Indeed, whereas cosmological theories have made great progress in their ability to predict the distribution of dark matter in the Universe, either analytically or numerically (e.g. Lacey & Cole 1993; Jenkins et al. 1998), the luminous properties of matter are much more difficult to model. For example, to relate the X-ray data of a cluster to its mass, a redshift-dependent luminosity-temperature relation needs to be employed (see Borgani et al. 1999 and references therein), in the absence of a detailed understanding of the physics in the intra-cluster gas. It would therefore be of considerable interest to be able to define a sample of ‘clusters’ – or more precisely, dark matter halos – which can be directly compared with the predictions coming from N-body simulations.

Weak gravitational lensing offers an attractive possibility to detect dark matter halos by their mass properties alone. A mass concentration produces a tidal gravitational field which distorts the light bundles from background sources. Owing to their assumed random intrinsic orientation, this tidal field can be detected statistically as a coherent tangential alignment of galaxy images around the mass concentration. A method to quantify this tangential alignment was originally introduced by Kaiser et al. (1994) to obtain lower bounds on cluster masses, and later generalized and proposed as a tool for the search of dark matter halos (Schneider 1996). This so-called aperture mass method can be applied to blank field imaging surveys to detect peaks in the projected density field. Combining halo abundance predictions from Press & Schechter (1974) theory with the universal density profile found in N-body simulations (Navarro et al. 1997), Kruse & Schneider (1999) estimated the number density of dark matter halos detectable with this method (with a signal-to-noise threshold of 5) to be of order  $10 \text{ deg}^{-2}$ , for a number density of 30 galaxies/arcmin<sup>2</sup>, and depending on the cosmological model. These predictions were confirmed (Reblinsky et al. 1999) by ray-tracing simulations (Jain et al. 1999) through numerically-generated cosmic density fields.

In this paper, we report the first detection of a dark matter halo not obviously associated with light, using the above-mentioned weak lensing technique. Using a  $14' \times 14'$  deep *V*-band image, obtained with MOCAM at CFHT, we aimed to investigate the projected mass profile of the cluster Abell 1942 on which the image is centered. We found a highly significant peak in the reconstructed mass map, in addition to that corresponding to the cluster itself. This second peak, located about  $7'$  South of the cluster center, shows up in the alignment statistic of background galaxy images with a significance  $> 99.99\%$ , as obtained from Monte-Carlo simulations which randomized the orientation of these background galaxies. An additional deep *I*-band image, taken with the UH8K at CFHT, confirms the presence of the mass peak. No obvious large overdensity of galaxies is seen at this location, implying either a mass concentration with low light-to-mass ratio, or a halo at substantially higher redshift than A1942 itself. Finally, an analysis of an archival

ROSAT/HRI image of A1942 shows, in addition to the emission from the cluster, a  $3.2\text{-}\sigma$  detection of a source with position close to the peak in the projected mass maps; though this weak detection would be of no significance by itself, the positional coincidence with the ‘dark’ clump suggests that it could correspond to the same halo, and that it may be due to a high-redshift ( $z \gtrsim 0.5$ ) cluster.

The outline of the paper is as follows: in Sect. 2 we describe the observations and data reduction techniques, as well as the measurement of galaxy ellipticities which we employed. The aperture mass statistic is briefly described in Sect. 3.1 and applied to the optical data sets, together with a determination of the peak detection significance. Properties of the mass concentration as derived from the optical data sets and the X-ray data are discussed in Sects. 3.2 and 3.3, respectively, and a discussion of our findings is provided in Sect. 4. In this paper we shall concentrate mainly on the ‘dark’ clump; an analysis of the mass profile of the cluster A1942 and the reliability of mass reconstruction will be published elsewhere (van Waerbeke et al., in preparation)

## 2. Summary of optical observations and image processing

The *V*- and *I*-band observations were obtained at the prime focus of CFHT with the MOCAM and the UH8K cameras, respectively. Both observing procedures were similar, with elementary exposure time of 1800 seconds each in *V* and 1200 seconds in *I*. A small shift of 10 arc-seconds between pointings was applied in order to remove cosmic rays and to prepare a super-flatfield.

The *V*-band images were obtained during an observing run in dark time of June 1995 with the  $4K \times 4K$  mosaic camera MOCAM (Cuillandre et al. 1997). Each individual chip is a  $2K \times 2K$  LORAL CCD, with  $0''.206$  per pixel, so the total field-of-view is  $14' \times 14'$ . Nine images have been re-centered and co-added, to produce a final frame with a total exposure time of 4h30min. The seeing of the coadded image is  $0''.74$ .

The *I*-band images were obtained with the  $8K \times 8K$  mosaic camera UH8K (Luppino et al. 1994). Each individual chip is a  $2K \times 4K$  LORAL CCD, also with  $0''.206$  per pixel, giving a field-of-view of  $28' \times 28'$ . The final centered coadded image resulting from 9 sub-images has a total exposure time of 3h and a seeing of  $0''.67$ . The *V*- and *I*-band images have been processed in a similar manner, using standard IRAF procedures and some more specific ones developed at CFHT and at the TERAPIX<sup>1</sup> data center for large-field CCD cameras. None of these procedures had innovative algorithms, so there is basically no difference in the pre-processing and processing of the MOCAM and UH8K images. For the present paper, we use only Chip 3 of the UH8K *I*-band image which contains the cluster A1942, and the additional mass concentration discussed further below. Fig. 1 shows the CCD images from both fields and their relative geometry.

A first object detection and the photometry have been performed with SExtractor2.0.17 (Bertin & Arnouts 1996). The

<sup>1</sup> <http://terapix.iap.fr>

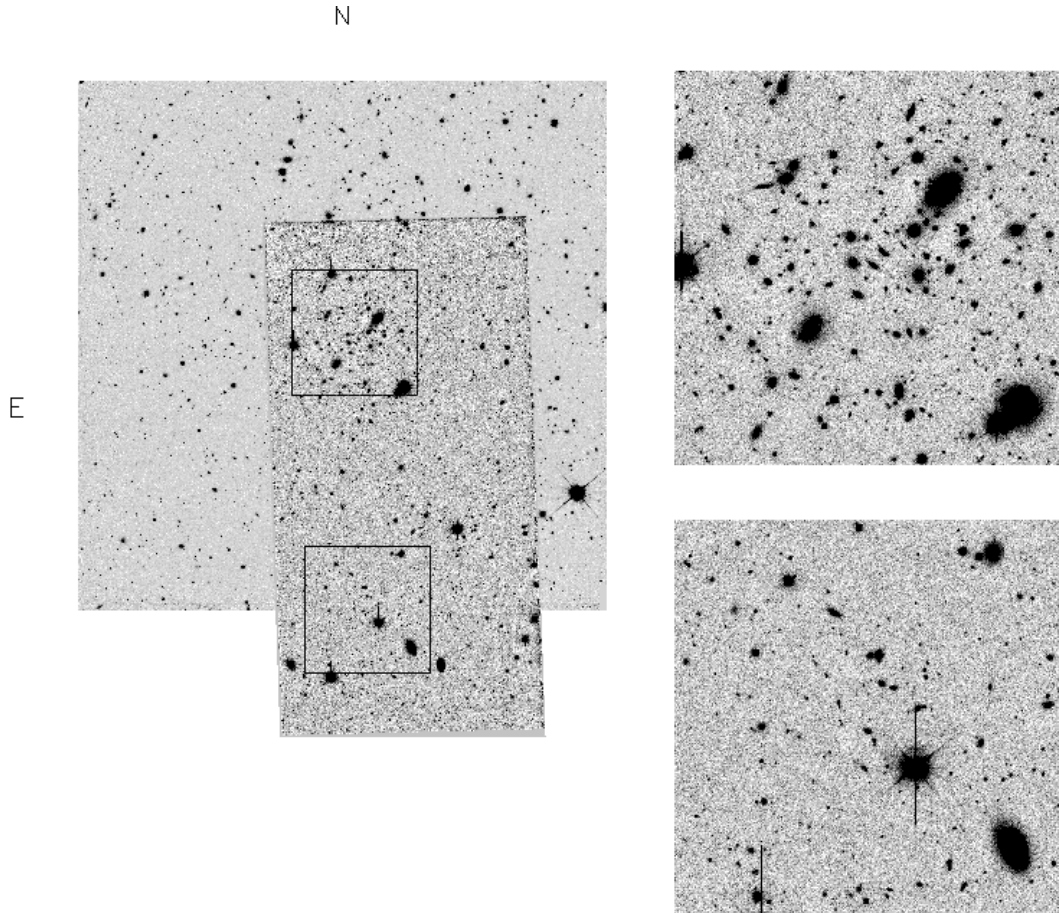


**Fig. 1.** The geometry of the optical data used in this paper. The left-hand side shows the area of the V-band MOCAM field (square) and the I-band UH8K-chip3 data (rectangle). The framed regions are  $3'.3 \times 3'.3$  cutouts around the cluster center of A1942 and around our ‘dark clump’ candidate. These regions are zoomed in on the right-hand side. The ‘dark clump’ region is centered around  $\alpha(J2000)=14^{\text{h}} 38^{\text{m}} 22.59^{\text{s}}$ ;  $\delta(J2000)=03^{\circ} 32' 32.22''$ .

MOCAM field has been calibrated using the photometric standard stars of the Landolt field SA110 (Landolt 1992), and the UH8K field was calibrated using the Landolt fields SA104 and SA110. The completeness limit is  $V = 26$  and  $I = 24.5$ .

The lensing analysis was done with the *imcat* software, based on the method for analysing weak shear data by Kaiser et al. (1995), with modifications described in Luppino & Kaiser (1997) and Hoekstra et al. (1998; hereafter HFKS98). This method is based on calculations of weighted moments of the light distribution. *Imcat* is specifically designed for the measurement of ellipticities of faint and small galaxy images, and their correction for the smearing of images by a PSF, and for any anisotropy of the PSF which could mimic a shear signal. These corrections are employed by the relation

$$\chi = \chi^0 + P^\gamma \gamma + P^{\text{sm}} p, \quad (1)$$

where  $\chi$  is the observed image ellipticity (defined as in, e.g. Schneider & Seitz 1995),  $\chi^0$  is the ellipticity of the unlensed source smeared by the isotropic part of the PSF,  $P^\gamma$  is the response tensor of the image ellipticity to a shear, and  $P^{\text{sm}}$  is the response tensor to an anisotropic part of the PSF, characterized by  $p$ . These tensors are calculated for each galaxy image individually. Since the expectation value of  $\chi^0$  in (1) is zero, one obtains an unbiased estimate of the shear through

$$\hat{\gamma} = (P^\gamma)^{-1} [\chi - P^{\text{sm}} p]. \quad (2)$$

( $\hat{\gamma}$  is in reality an estimate for the reduced shear  $\gamma/(1 - \kappa)$  which reduces to the shear if  $\kappa \ll 1$ .) The PSF anisotropy in our images is fairly small and regular over the field. We selected bright, unsaturated stars from a size vs. magnitude plot (see Fig. 2) and determined their ellipticities. As Fig. 3 shows, the stellar ellipticity changes very smoothly over the fields so that its behaviour can be easily fit with a second-order polynomial (see also Fig. 4). With these polynomials we performed the anisotropy correction in (1). We follow the prescription of HFKS98 for the calculation of  $P^\gamma$ , and used the full tensors, not just their trace-part, in (2).

The current version of *imcat* does not give information about the quality of objects; for this we produced a SExtractor (version 2.0.20) catalog containing all objects that had at least six connected pixels with  $1-\sigma$  above the local sky background. From this catalog we sorted out all objects with potential problems for shape estimation (like being blended with another object or having a close neighbour). This included all objects with  $\text{FLAGS} \geq 2$  (internal SExtractor flag). The remaining catalog was matched with the corresponding *imcat* catalog, using a maximum positional difference of three pixels, and keeping only those objects for which the detection signal-to-noise of *imcat* was  $\geq 7$ .

This procedure left us with 4190 objects ( $V > 22.0$ ) for the MOCAM and 1708 objects ( $I > 21.0$ ) for the I-band chip3. With these final catalogs all subsequent analysis was done. We

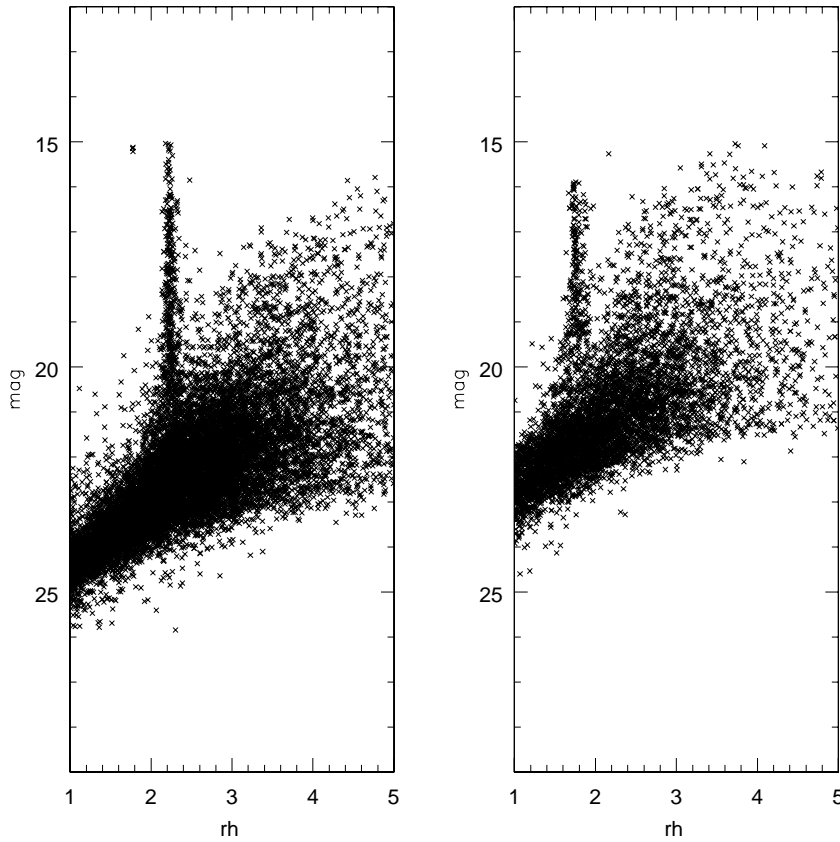


**Fig. 2.** For all objects detected with the imcat method from the MOCAM frame (left panel) and the UH8K chip3 (right panel), the magnitude is plotted as a function of half-light radius  $r_h$ , measured in pixels. Objects containing saturated pixels have been removed from the plots. The magnitudes are in an arbitrary system. In both cases we can clearly identify a prominent sequence of stellar objects at about  $r_h = 2.2$  for MOCAM, and  $r_h = 1.75$  for UH8K-chip3.

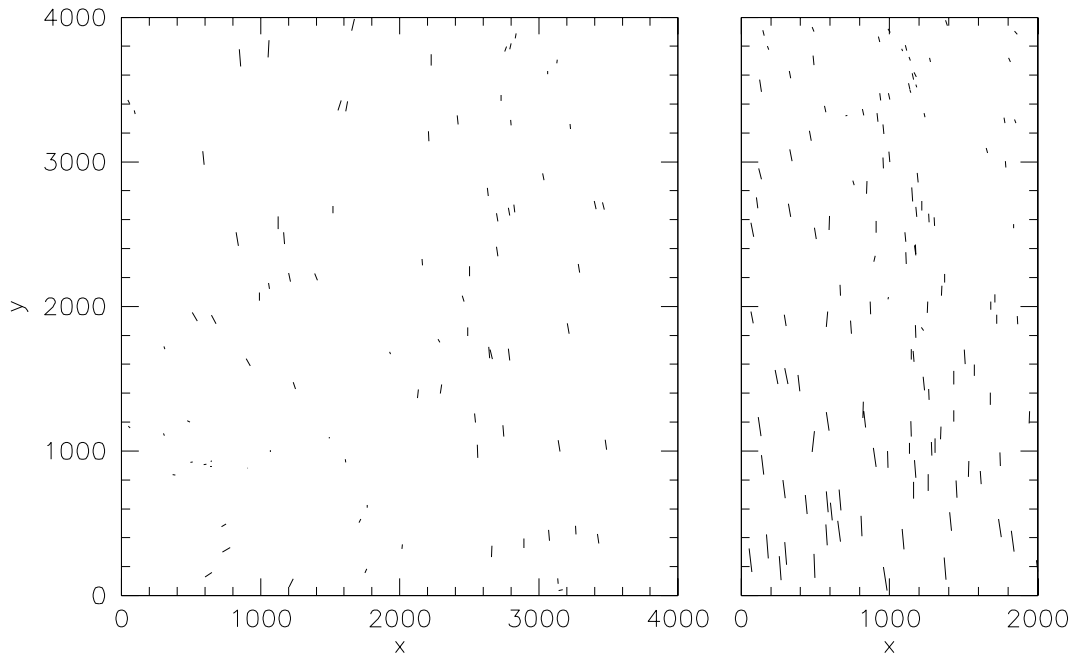


**Fig. 3.** The ellipticity fields for stars for the  $V$ -band MOCAM field (left panel) and the  $I$ -band UH8K-chip3 containing the cluster. Both fields show a smooth variation and can be easily modelled by a low-order polynomial. The maximal ellipticity is about 5% for the MOCAM and 8% for the UH8K.

note that we did not cross-correlate the MOCAM and UH8K catalogs; hence, the galaxies taken from both catalogs are not exactly the same, even in the region of overlap. Due to the different waveband used for object selection, the redshift distribution of the background galaxies selected on the MOCAM and the UH8K-chip3 frame can be different.

### 3. Analysis of the ‘dark’ clump

#### 3.1. Weak lensing analysis

From the image ellipticities of ‘background’ galaxies, we have first reconstructed the two-dimensional mass map of the cluster field from the MOCAM data, using the maximum-likelihood method described in Bartelmann et al. (1996) and indepen-

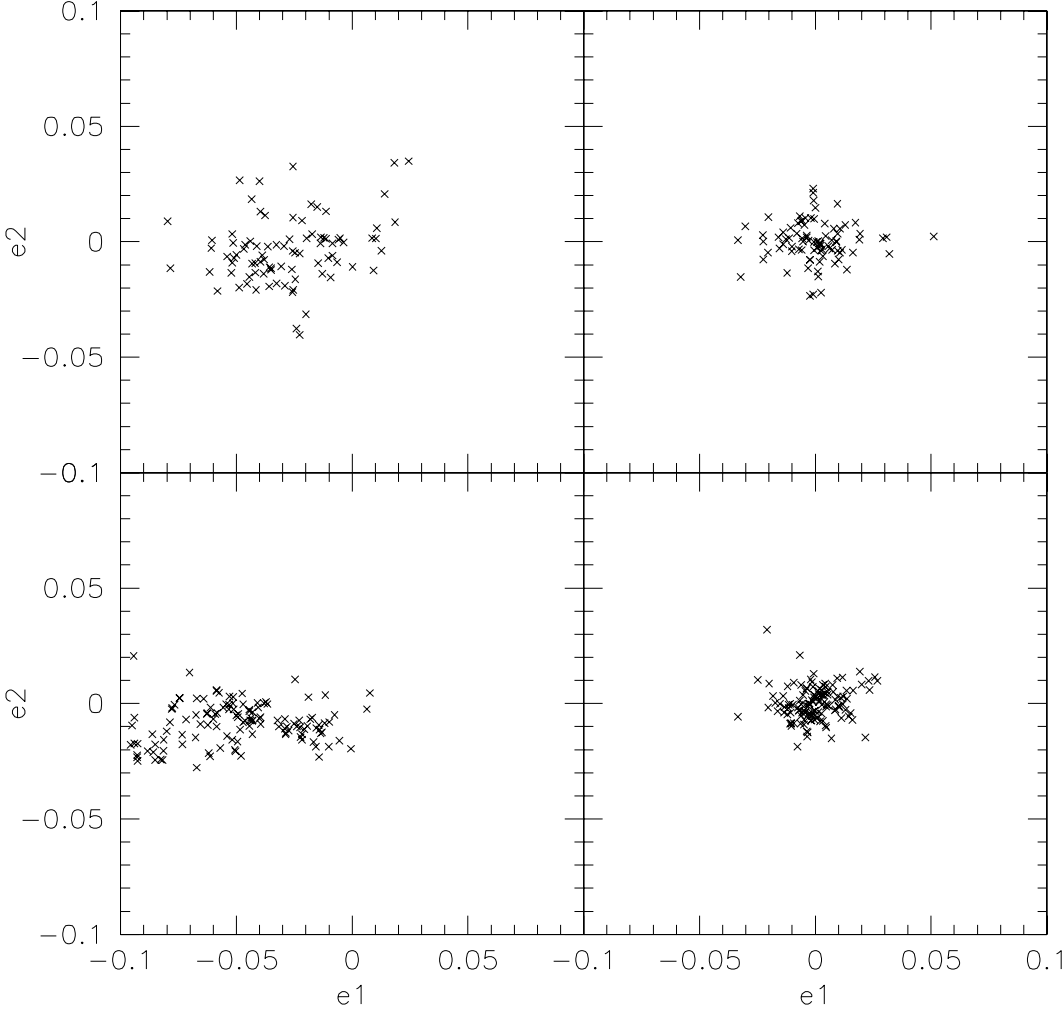


**Fig. 4.** The left panels show the raw imcat ellipticities from bright, unsaturated foreground stars in our fields (upper panels: MO-CAM field; lower panels: UH8K chip). The right panels show the ellipticities after they have been corrected with a second-order polynomial as described in the text. The rms of the ellipticities after correction is typically 0.015.

dently, the method described in Seitz & Schneider (2000). The resulting mass maps are very similar, and we show the former of these only.

In the left panel of Fig. 5, we show the resulting mass map with the (mass-sheet degeneracy) transformation parameter  $\lambda$  chosen such that  $\langle \kappa \rangle = 0$  (see Schneider & Seitz 1995), together with contours of the smoothed number density of bright galaxies. In general, this number density correlates quite well with the reconstructed surface mass density. As can be seen, a prominent mass peak shows up centered right on the brightest cluster galaxy.

In addition to this mass peak, several other peaks are present in the mass map. Such peaks may partly be due to noise coming from the intrinsic image ellipticities and, to a lesser degree, to errors in the determination of image ellipticities. In order to test the statistical significance of the mass peaks, we used the aperture mass method (Schneider 1996).

Let  $U(\vartheta)$  be a filter function which vanishes for  $\vartheta \geq \theta$ , and which has zero mean,  $\int_0^\theta d\vartheta \vartheta U(\vartheta) = 0$ . Then we define the aperture mass  $M_{\text{ap}}(\vartheta)$  at position  $\vartheta$  as

$$M_{\text{ap}}(\vartheta) = \int_{|\vartheta'| \leq \theta} d^2\vartheta' \kappa(\vartheta + \vartheta') U(|\vartheta'|). \quad (3)$$

Hence,  $M_{\text{ap}}(\vartheta)$  is a filtered version of the density field  $\kappa$ ; it is invariant with respect to adding a homogeneous mass sheet or a linear density field, and is positive if centered on a mass peak with size comparable to the filter scale  $\theta$ . The nice feature about this aperture mass is that it can be expressed directly in terms of the shear, as

$$M_{\text{ap}}(\vartheta) = \int_{|\vartheta'| \leq \theta} d^2\vartheta' \gamma_t(\vartheta'; \vartheta) Q(|\vartheta'|) \quad (4)$$

(Kaiser et al. 1994; Schneider 1996), where the filter function  $Q(\vartheta) = 2\vartheta^{-2} \int_0^\vartheta d\vartheta' \vartheta' U(\vartheta') - U(\vartheta)$  is determined in terms of  $U(\vartheta)$ , and vanishes for  $\vartheta \geq \theta$ . We use the functions  $U$  and  $Q$  given in Schneider et al. (1998) with  $l = 1$  (Eqs. (3.12) and (3.13) in their paper). The tangential shear  $\gamma_t(\vartheta'; \vartheta)$  at relative position  $\vartheta'$  with respect to  $\vartheta$  is defined as

$$\gamma_t(\vartheta'; \vartheta) = -\mathcal{R}e[\gamma(\vartheta + \vartheta') e^{-2i\varphi'}], \quad (5)$$

where  $\varphi'$  is the polar angle of the vector  $\vartheta'$ . In the case save of weak lensing ( $\kappa \ll 1$ ), the observed image ellipticities  $\hat{\gamma}$  from (2) are an unbiased estimator of the local shear, and so the aper-

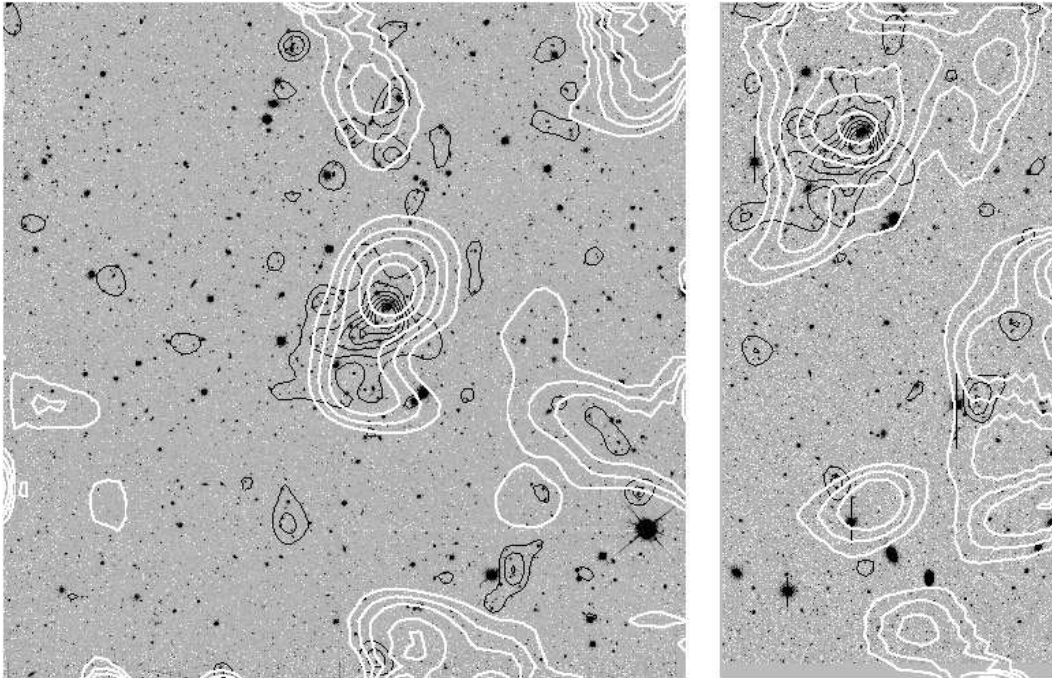


**Fig. 5.** The figure shows mass reconstructions and galaxy number density from the MOCAM field (left panel) and the UH8K-chip3 (right panel). The white contours show  $\kappa = 0.03, 0.05, 0.07, 0.1, 0.12, 0.15, 0.17$  and  $0.2$ . For the reconstruction the shear was smoothed with a Gaussian of  $\sigma = 40''$  width. The black contours show the smoothed galaxy distribution from all galaxies brighter than  $V = 21.0$  and  $I = 20.0$  (the smoothing kernel here was a Gaussian with  $\sigma = 20''$ ).

ture mass can be obtained by summing over image ellipticities as

$$M'_{\text{ap}}(\vartheta) = \frac{\pi\theta^2}{N} \sum_i \hat{\gamma}_{ti}(\vartheta) Q(|\theta_i - \vartheta|), \quad (6)$$

where the sum extends over all  $N$  galaxy images with positions  $\theta_i$  which are located within  $\theta$  of  $\vartheta$ , and the tangential component  $\hat{\gamma}_{ti}(\vartheta)$  of the image ellipticity relative to the position  $\vartheta$  is defined in analogy to  $\gamma_t$ . In general,  $M'_{\text{ap}}(\vartheta)$  is not an unbiased estimator of  $M_{\text{ap}}(\vartheta)$  since the expectation value of  $\hat{\gamma}$  is the reduced shear, not the shear itself. However, unless the aperture includes a strong mass clump where  $\kappa$  is not small compared to unity,  $M'_{\text{ap}}$  will approximate  $M_{\text{ap}}$  closely. But even if the weak-lensing approximation breaks down for part of the aperture, one can consider the quantity  $M'_{\text{ap}}(\vartheta)$  in its own right, representing the tangential alignment of galaxy images with respect to the point  $\vartheta$ . This interpretation also remains valid if the aperture is centered on a position which is less than  $\theta$  away from the boundary of the data field, so that part of the aperture is located outside the data field, in which case  $M'_{\text{ap}}(\vartheta)$  will not be a reliable estimator of  $M_{\text{ap}}(\vartheta)$ .

In order to determine the significance of the peaks in the mass map shown in Fig. 5, we have calculated  $M'_{\text{ap}}$  on a grid of points  $\vartheta$  over the data field, for four values of the filter scale  $\theta$ . Then, we have randomized the position angles of all galaxy images, and calculated  $M'_{\text{ap}}$  on the same grid for these randomized realizations. This has been repeated  $N_{\text{rand}}$  times. Finally, at each grid point the fraction  $\nu$  of randomizations where  $M'_{\text{ap}}$  is larger than the measured value from the actual data has been obtained; this fraction (which we shall call ‘error level’ in the following) is the probability of finding a value of  $M'_{\text{ap}}$  at that gridpoint for randomly oriented galaxy images, but with the same positions and ellipticities as the observed galaxies.

Fig. 6 displays the contours of constant  $\nu$ , for different filter radii, varying from  $80''$  to  $200''$ . As can be seen, the cluster center shows up prominently in the  $\nu$ -map on all scales. In addition, two highly significant peaks show up, one at the upper right corner, the other  $\sim 7'$  South of the cluster center, close to the edge of the MOCAM field. We have verified the robustness of this Southern peak by using SExtractor ellipticities instead of those from imcat, and found both the cluster components and the Southern peak also with that catalog (although it should be much less suited for weak lensing techniques).

After these findings, we obtained the UH8K  $I$ -band image, on which both the cluster and the Southern mass peak are located on Chip 3. The mass reconstruction from galaxy images on Chip 3 are shown in the right panel of Fig. 5, from which we see that the cluster and this Southern mass peak also show up. Repeating the aperture mass statistics for Chip 3, we obtain the error levels as shown in Fig. 7; again, this Southern peak shows up at very high significance. There is a third peak, about halfway between the cluster and the Southern component and slightly to the West, which also seems also quite significant for the largest smoothing scale. However as shown in Fig. 7 the significance is highly sensitive to the smoothing scale, which is an indication for a not very strong mass concentration at this position, if it even exists. In fact we show later in Sect. 3.2 that this third peak is not significant enough to conclude that a mass overdensity exists here. Therefore, we shall concentrate on the Southern peak, which we call, for lack of a better name, the ‘dark clump’.

In fact, as can be seen from Figs. 1 and 5, this mass peak does not seem to be associated with any concentration of brighter galaxies. This could mean two things: either, the mass concentration is in fact associated with little light, or is at much higher redshift than A1942 itself.

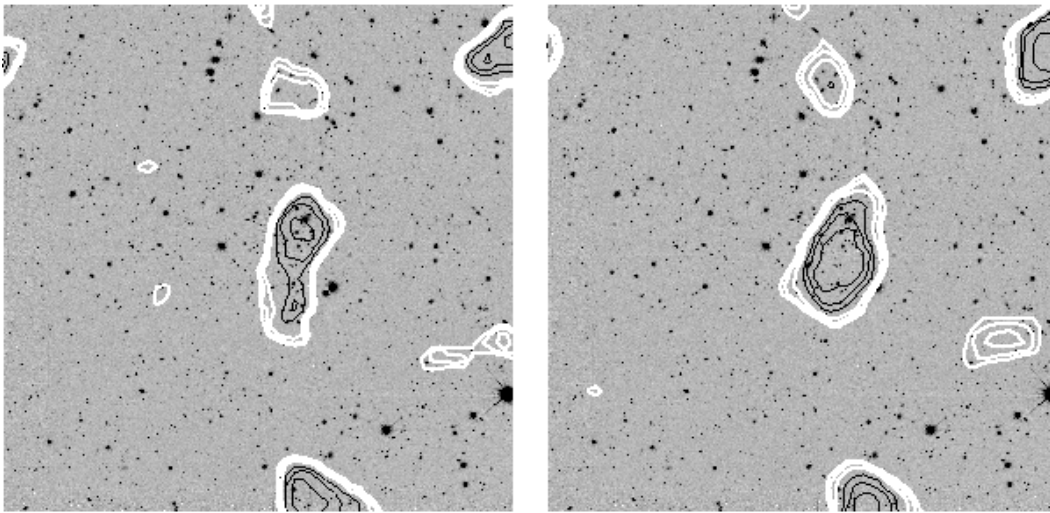
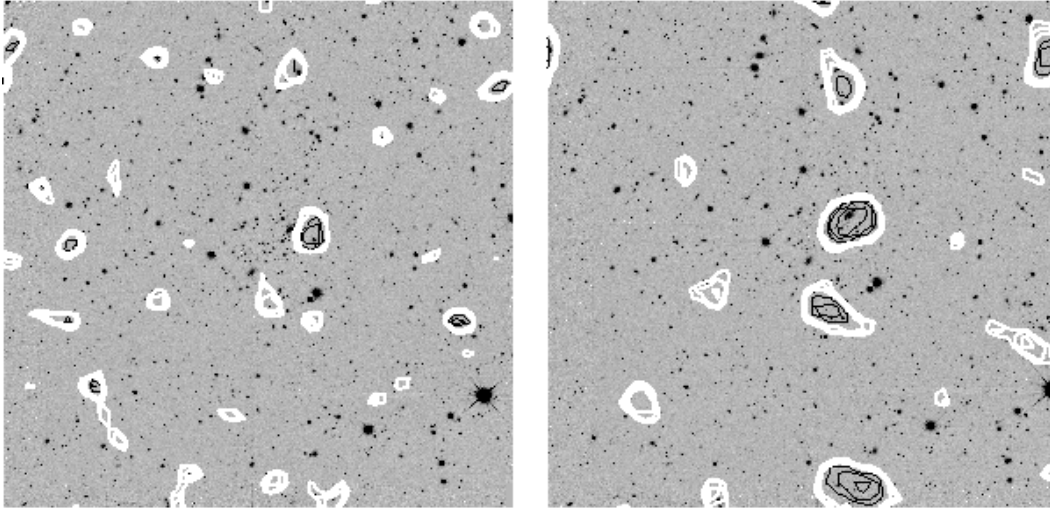


**Fig. 6.** The four panels show the significance  $\nu$  (see text) of the  $M'_{\text{ap}}$  maps of the MOCAM field. We chose  $N_{\text{rand}} = 5000$ , the black contours mark areas with  $\nu = 1, 10, 30/5000$  and the white contours  $\nu = 100, 180, 260/5000$ . The filter scales are  $80''$  (upper left panel),  $120''$  (upper right panel),  $160''$  (lower left panel) and  $200''$  (lower right panel). For the larger scales the cluster components and the dark clump are detected with a very high significance.

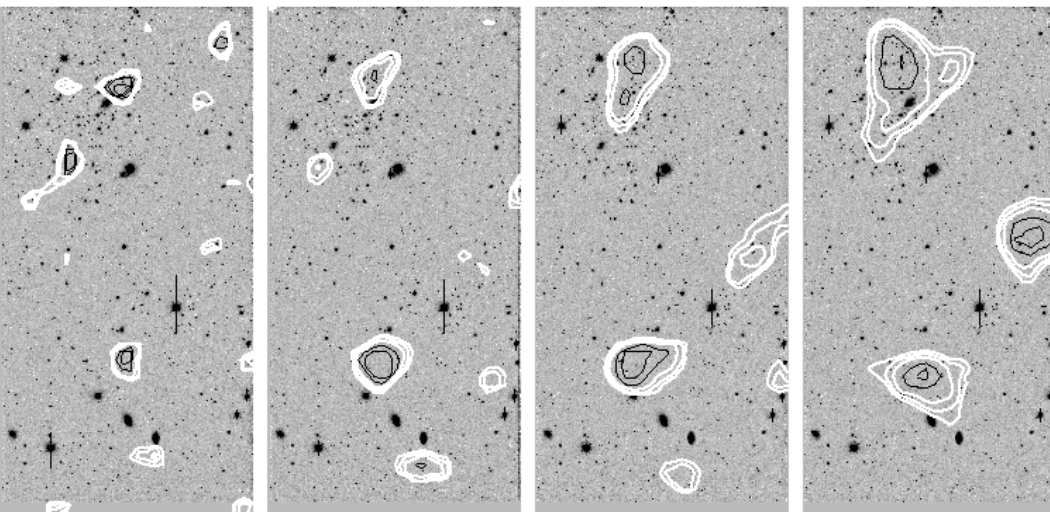


**Fig. 7.** The same as Fig. 6 for the UH8K-chip3  $I$ -band data. The filter scales are, from left to right:  $80''$ ,  $120''$ ,  $160''$  and  $200''$ . A1942 and the dark clump are also detected here with a very high significance.

Concentrating on the location of the dark clump, we determined the probability distribution  $p_0(M'_{\text{ap}})$  for the value of  $M'_{\text{ap}}$ , obtained from  $2 \times 10^6$  randomizations of the galaxy orientations within  $160''$  of the dark clump. This probability distribution is

shown as the solid (from MOCAM) and dashed (from Chip 3) curve on the left of Fig. 8. These two distributions are very well approximated by a Gaussian, as expected from the central limit theorem. The value of  $M'_{\text{ap}}$  at the dark clump is 0.0395 for MO-



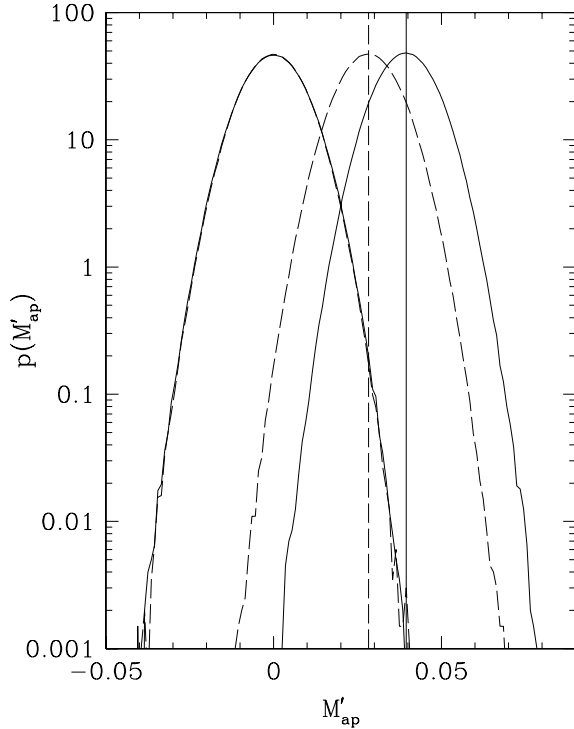


**Fig. 8.** Probability distributions for  $M'_{\text{ap}}$ , with the aperture centered on the peak position of the dark clump. Solid (dashed) curves correspond to the MOCAM (Chip 3) data set. For an aperture of  $160''$ , the left of the two curves shows the probability distribution  $p_0(M'_{\text{ap}})$  for values of  $M'_{\text{ap}}$  obtained by randomizing the position angles of the galaxy images. These two curves nearly coincide. The two curves on the right-hand side show the probability distribution  $p_{\text{boot}}(M'_{\text{ap}})$  obtained from bootstrap resampling of the galaxy images inside the aperture. The two vertical lines show the measured values of  $M'_{\text{ap}}$ .

CAM, and 0.0283 for Chip 3. The fact that these two values are different is not problematic, since for Chip 3, the whole aperture fits inside the data field, whereas it is partially outside for MOCAM; hence, the two values of  $M'_{\text{ap}}$  measure a different tangential alignment. Also, since the two data sets use galaxies selected in a different waveband, their redshift distribution can be different, yielding different values of the resulting lens strength. The probability that a randomization of image orientations yields a value of  $M'_{\text{ap}}$  larger than the observed one, at that position, is  $\sim 10^{-6}$  for the MOCAM field, and  $4.2 \times 10^{-4}$  for Chip 3.

Next we investigate whether the highly significant value of  $M'_{\text{ap}}$  at the dark clump comes from a few galaxy images only. For this, the sample of galaxy images inside the aperture was bootstrap resampled, to obtain the probability  $p_{\text{boot}}(M'_{\text{ap}})$  that this resampling yields a particular value of  $M'_{\text{ap}}$ . This probability is also shown in Fig. 8. The probability that the bootstrapped value of  $M'_{\text{ap}}$  is negative is  $3.8 \times 10^{-4}$  for Chip 3, and  $< 10^{-6}$  for the MOCAM peak.

The radial dependence of the tangential image ellipticity is considered next. Fig. 9 shows the mean tangential image ellipticity in annuli of width  $20''$ , both for the MOCAM and the UH8K data centered on the dark clump. The error bars show the

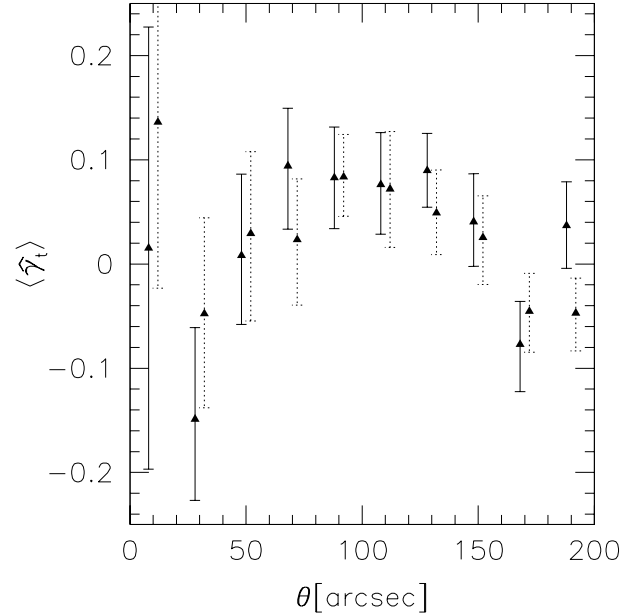


**Fig. 9.** Mean tangential image ellipticity in independent bins of width  $20''$  around the dark clump, triangles show the mean, solid (dashed) error bars the 80% error interval obtained from bootstrapping, using the MOCAM (Chip 3) data. For better display, the points and error bars are slightly shifted in the  $\theta$  direction.

80% probability interval obtained again from bootstrapping. It is reassuring that the radial behaviour of  $\langle \hat{\gamma}_t \rangle$  is very similar on the two data sets. In fact, owing to the different wavebands of the two data fields and the fact that the aperture does not fit inside the MOCAM field, this agreement is better than one might expect. The mean tangential ellipticity is positive over a large angular range; except for one of the inner bins (for which the error bar is fairly large),  $\langle \hat{\gamma}_t \rangle$  is positive in all bins for  $\theta \lesssim 150''$ . This figure thus shows that the large and significant value of  $M'_{\text{ap}}$  at the dark clump is not dominated by galaxy images at a particular angular separation.

### 3.2. Significance of the third clump

So far we have focussed on the probability to find a value of  $M_{\text{ap}}$  larger than the observed value at a given location. No case was made about the fact that we preselected a peak at that location. However it was shown (Van Waerbeke 1999) that the probability to get by chance a peak of given height is higher than the probability to get the same value for  $M_{\text{ap}}$  in the field. Therefore, when we ask the question “what is the significance of such-and-such a peak?”, we have to calculate the significance according to the peak probability distribution function (pdf) in addition to the one calculated with the field points pdf. It will provide the significance of the peak itself, in addition to the significance of the pixel value. This leads to an alternative determination of the significance of the clumps using the method developed in Van Waerbeke (1999). The author showed that, for a Gaussian smoothing, the noise in mass maps behaves essentially like a 2-

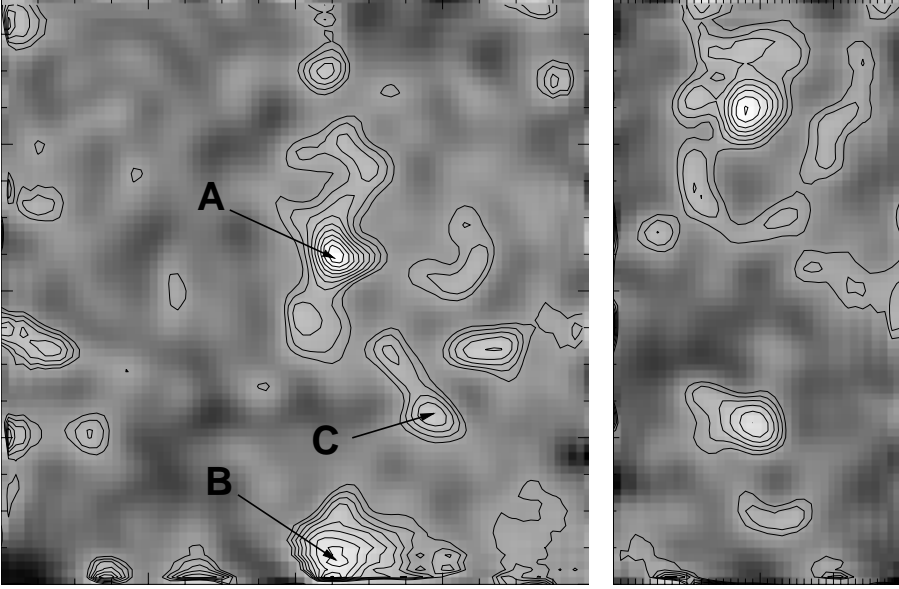


**Fig. 10.** Mass maps for the MOCAM and the UH8K-chip3 fields with a smoothing scale of  $64''$ . The  $\kappa$  contours are  $1\sigma_0, 1.5\sigma_0, 2\sigma_0, 2.5\sigma_0, \dots$  where  $\sigma_0$  is the zero-lag variance of the convergence ( $\sigma_0 = 0.045$  for MOCAM and  $\sigma_0 = 0.047$  for UH8K-chip3, see details in the text). The A1942 cluster is A, the dark clump is B and the less significant third clump is C.

**Table 1.** Significance of the main clumps (A,B,C on Fig. 8) for the MOCAM and the UH8K-chip3 fields using the mass map of Fig. 10. We indicate the signal-to-noise ratio as a function of  $\sigma_0$  ( $\sigma_0^2$  is by definition the zero-lag value of the noise correlation function (7)), and between parentheses the probability that the peak height might have a higher value than the one observed due to the noise fluctuations. These numbers correspond to a smoothing radius of  $\mathcal{R}_0 = 32''$ , which was chosen in order to maximize the peak’s significance.

Peak #	MOCAM $\sigma_0 = 0.045$	UH8K-chip3 $\sigma_0 = 0.047$
A (A1942)	5.4 ( $1.7 \times 10^{-6}$ )	4.5 ( $1.2 \times 10^{-4}$ )
B (Dark clump)	4.5 ( $1.2 \times 10^{-4}$ )	3.5 ( $5.3 \times 10^{-3}$ )
C	2.8 ( $3.9 \times 10^{-2}$ )	1.5 (0.40)

dimensional Gaussian random field whose 2-point correlation function  $\langle N(\boldsymbol{\theta})N(\boldsymbol{\theta}') \rangle$  is given by:

$$\langle N(\boldsymbol{\theta})N(\boldsymbol{\theta}') \rangle = \frac{\sigma_\epsilon^2}{2} \frac{1}{2\pi\mathcal{R}_0^2 n_g} \exp - \left( \frac{|\boldsymbol{\theta}' - \boldsymbol{\theta}|^2}{2\mathcal{R}_0^2} \right), \quad (7)$$

where  $\sigma_\epsilon$  is the galaxy ellipticity variance (Note that here  $\sigma_\epsilon$  is defined as the variance of the vector ellipticity, not the variance of its modulus as it is usually the case).  $n_g$  is the number density of the galaxies, and  $\mathcal{R}_0$  the radius of the gaussian smoothing window. We can then assign to each mass peak the probability that it is a pure noise fluctuation using Gaussian peak statistics (Bond & Efstathiou 1987). Since it is not yet demonstrated that the noise model works for a compensated filter, we use a mass reconstruction using a Gaussian filter on MOCAM and UH8K-Chip3 in order to estimate the peak significance. Fig. 10 shows the three major peaks visible in both MOCAM and UH8K-chip3 fields on these maps.

Table 1 shows the significance for these peaks. As expected from Van Waerbeke (1999), the probabilities found with the

peak statistic are smaller than the probabilities found with the field statistic obtained from the bootstrap resampling described in Sect. 3.1. Fortunately, the main cluster A and the dark clump B remain highly significant, however the peak C is not that significant. The results of the  $M_{\text{ap}}$  statistic in Fig. 7 show that the significance of the peak C is highly unstable with the smoothing scale. We conclude that even if we cannot reject the existence of a mass peak at that location, it is certainly too noisy to allow a reliable analysis, and we decided to discard the third clump for the rest of the analysis.

### 3.3. Significance of the centroid’s position

Another useful information is the dispersion of the measured centroid of the dark clump (and A1942). This is important for instance in Sect. 3.4 where we compare the dark clump centroid position with the position of a nearby compact X-ray source. The best way for measuring the dispersion of a centroid would be to use a parametric model for the mass concentration and generate many noisy mass reconstructions with different galaxy ellipticities and positions. The dispersion would then be correctly measured among those different mass reconstructions. Unfortunately such a parametric model is not available and the best we can do is to consider the reconstructed mass map from the data as the mass model itself. We can then generate as many noise maps as we want using the noise model outlined in Sect. 3.2 (see Van Waerbeke 1999) and add them to the *mass model*. A noise map is a two-dimensional Gaussian random field with a correlation function given by (7). The same approach was used in Athreya et al. (2000) where the authors estimated the significance of the center of mass with respect to the center of light.

Fig. 11 shows the centroid dispersion for A1942 and the dark clump as measured using the UH8K-chip3 mass map of Fig. 10 as the “mass model”. The one sigma dispersion for A1942 is  $\sim 13.8''$ , and for the dark clump  $\sim 18''$ .

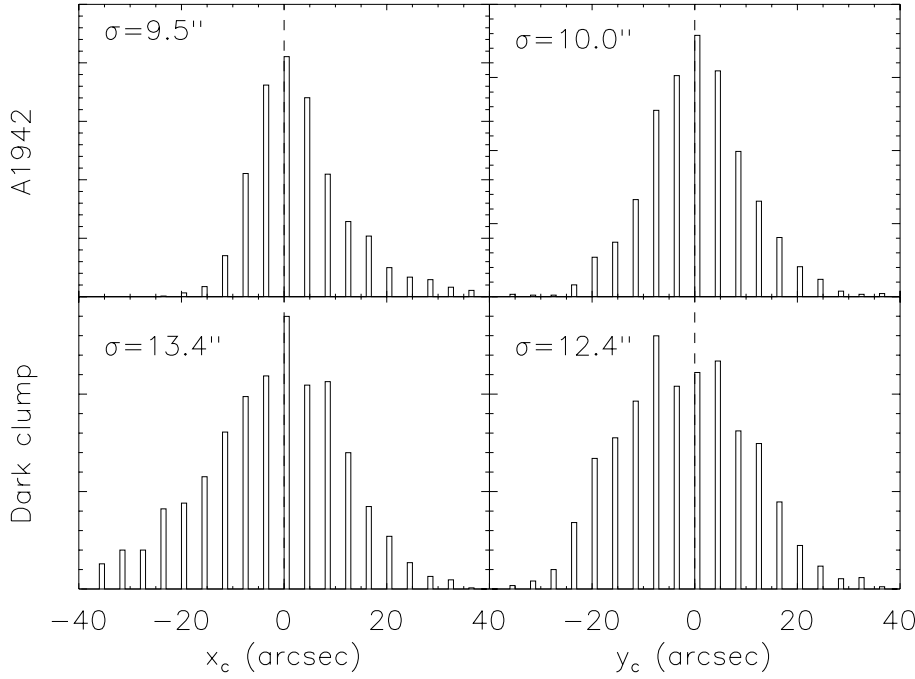


**Fig. 11.** Parametric bootstrap resampling of the centroid of A1942 (upper row) and the dark clump (lower row). The noise level is calculated according to the noise found in UH8K-chip3 of Fig. 8 ( $\mathcal{R}_0 = 32''$ ,  $\sigma_\epsilon = 0.36$ ,  $n_g \simeq 15 \text{ gal/arcmin}^2$ ). Note that  $\sigma_\epsilon$  is here the variance of the vector ellipticity, not the variance of the modulus of the ellipticity. The left column corresponds to the X-axis offset, and the right column to the Y-axis offset.  $\sigma$  indicates the  $1-\sigma$  dispersion of the different histograms. The bootstrap was done over 2000 realisations of the noise.

### 3.4. Properties of the dark clump

We now investigate some physical properties of our dark clump candidate. We first argue that it is very unlikely for our object to lie at a redshift higher than  $z_d = 1$ . For our magnitude limit of 24.5 in the  $I$  band we expect approximately 30 galaxies/ $(1')^2$ . We used approximately half of them (see Sect. 2) as putative background galaxies for our analysis. The median of simulated redshift distributions that extend the CFRS data (Lilly et al. 1995) to fainter magnitude limits (Baugh et al. 1996) is at about  $z \approx 0.7 - 0.8$ . If we assume that all our galaxies lie in the extreme tail of these distributions, then  $z = 1.0$  represents a good upper limit for the redshift of our clump. However, the lensing analysis of the high-redshift cluster MS1054–03 (Luppino & Kaiser 1997) may provide an indication for a somewhat larger mean source redshift.

Next we use Fig. 9 to obtain a crude estimate of the mass of this object. Although the tangential shear appears to be fairly small close to the center position of the clump, there is a region between  $\sim 50''$  and  $\sim 150''$  where the tangential shear is clearly positive and decreases smoothly with radius. If we describe the mass profile by an isothermal sphere, its velocity dispersion  $\sigma_v$  would be given by

$$\left(\frac{\sigma_v}{c}\right)^2 = \frac{1}{2\pi} (\gamma_t \theta) \left\langle \frac{D_{ds}}{D_s} \right\rangle^{-1}, \quad (8)$$

where the product  $\gamma_t \theta$  would be independent of  $\theta$  for an isothermal sphere model, and the final term is the ratio lens-source to observer-source distance, averaged over the background galaxy population. Introducing fiducial parameters, this becomes

$$\sigma_v = 1135 \sqrt{\frac{\gamma_{100}}{0.06}} \sqrt{\frac{1}{3 \langle D_{ds}/D_s \rangle}} \text{ km/s}, \quad (9)$$

where  $\gamma_{100}$  is the tangential shear  $100''$  from the mass center. Alternatively, we can express this result in terms of the mass within a sphere of radius  $R$ ,  $M(< R) = 2\sigma_v^2 R/G$ ; for example, within  $R = 0.5h^{-1} \text{ Mpc}$ , we find

$$M(< 0.5h^{-1} \text{ Mpc}) = 2.9 \times 10^{14} h^{-1} M_\odot \frac{\gamma_{100}}{0.06} \frac{1}{3 \langle D_{ds}/D_s \rangle}. \quad (10)$$

Whereas this model is quite crude, the largest uncertainty in quantitative mass estimates comes from the unknown redshift of the dark clump and the unknown redshift distribution of the background galaxy population. The mass is a monotonically increasing function of the lens redshift, and depends very strongly on the assumed mean source redshift, in particular for values of  $z_d \gtrsim 0.5$ .

With the  $I$ -band data we now estimate the light coming from the dark clump. For this we created a SExtractor catalog counting every connected area with at least 3 pixels  $0.5-\sigma$  above the sky background as a potential object. The flux of all these objects (except from obvious stars) in a circle of  $100''$  radius around the clump center was summed up. We did the same in 32 control circles around ‘empty’ regions in the other UH8K chips. It turned out that the flux within the clump region is compatible with the mean flux of the control annuli, i.e., there is no overdensity of light at the position of the dark clump. So we took the  $1-\sigma$  fluctuation of the fluxes in the control circles as a reasonable upper limit for the light coming from the dark clump. For converting the flux into a total  $I$ -band magnitude we assumed that we are dominated by elliptical galaxies, using  $K$  corrections for this galaxy type calculated with the latest version of the Bruzual & Charlot stellar population synthesis models for the spectrophotometric evolution of galaxies (Bruzual & Charlot 1993). From the total  $I$ -band magnitude we derived a bolo-

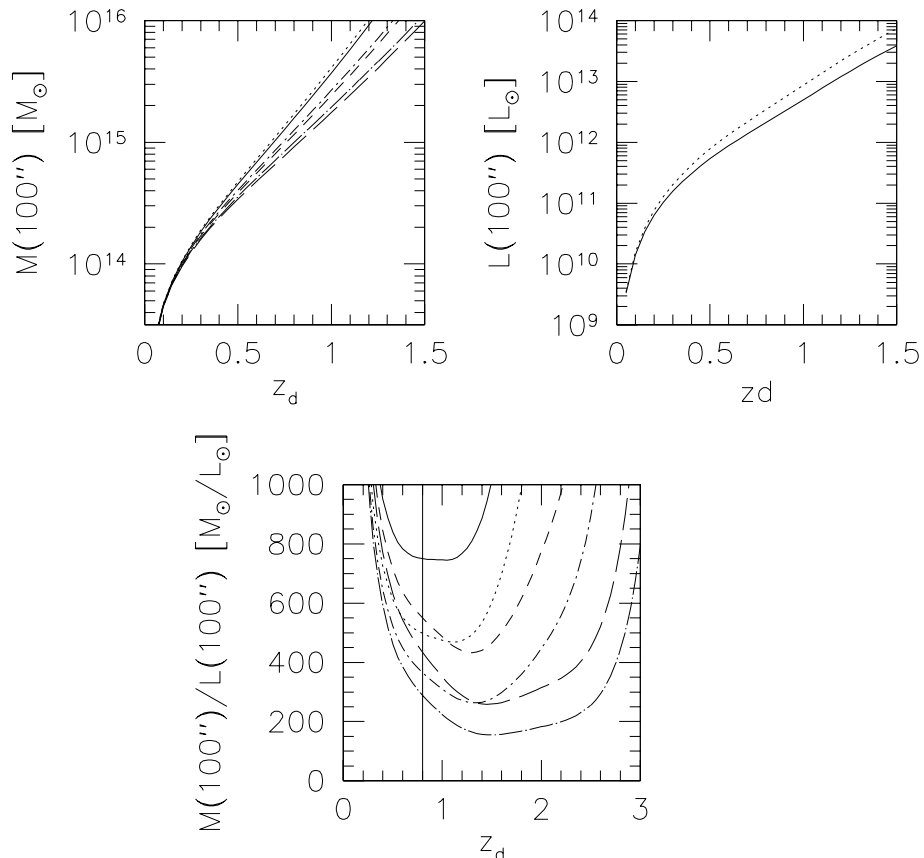


**Fig. 12.** Estimate of the lensing mass (upper left panel), an upper bound for the luminosity of the lens (upper right panel), and a lower limit on the mass-to-light ratio (lower panel), as a function of assumed lens redshift. All estimates are for an aperture size of  $100''$ . The solid, short dashed and long dashed curves show the  $M/L$  ratio in an EdS universe for  $\langle z_s \rangle = 0.8$ ,  $\langle z_s \rangle = 0.9$  and  $\langle z_s \rangle = 1.0$ . The dotted, dot-short dashed and dot-long dashed curves show the same in an  $\Omega = 0.3$ ,  $\Lambda = 0.7$  universe. We have assumed a redshift distribution  $\propto z^2 \exp[-(z/z_0)^{3/2}]$  for the source galaxies; hence  $\langle z_s \rangle \approx 1.5z_0$ . A value of  $\gamma_{100} = 0.06$  was used, which corresponds to the measured average tangential shear on Fig. 13 between  $50''$  and  $150''$ .

metric magnitude and a bolometric luminosity using standard approximations. With a lower limit for the mass and an upper limit for the luminosity we can give lower limits for the mass to light ratio of our object. This is shown in Fig. 12 for different source redshift distributions and two cosmologies. We see that the EdS universe gives fairly high  $M/L$  estimates in comparison to a  $\Omega = 0.3$ ,  $\Lambda = 0.7$  model. When we assume a redshift of  $z \approx 0.8$  for our clump we obtain a lower limit of  $M/L \approx 300$  in the  $\Lambda$  cosmology. This is a conservative lower limit which could be lowered significantly only if one assumes that the redshift distribution of the faint galaxies extends to substantially higher redshift.

As the dark clump may have a mass representative of massive clusters it is of interest to search for X-ray emission associated with it.

### 3.5. The X-ray data analysis

A1942 was observed by the ROSAT HRI in August 1995. The total integration time was 44,515 s. We retrieved the X-ray images from the public archive and reduced them using ESAS, Snowden's code especially developed for the analysis of extended sources in ROSAT data (Snowden et al 1994; Snowden & Kuntz 1998).

The region showing a significant peak in the weak lensing reconstructed mass map is within the field of view of the HRI image of A1942. We have searched for X-ray emission in this

area. First of all, we have refined the astrometry in the X-ray image matching X-ray point sources to objects in our deep optical images. The astrometric offset from the original instrument coordinates is  $3.5''$ . There is a significant X-ray emission peak centered at  $14^{\text{h}} 38^{\text{m}} 22.8^{\text{s}}$ ,  $3^{\circ} 33' 11''$  (J2000.0). This position is  $60''$  away from the weak lensing mass peak. The X-ray source is detected at the  $3.2\text{-}\sigma$  level using an aperture of  $30''$  radius. Although the number of counts detected is low, its distribution is inconsistent with a point-like source, showing a profile elongated along the NW-SE direction that is broader than the instrumental PSF.

We have measured the source count-rate using concentric circular apertures centered on the X-ray emission peak. We obtain a count-rate of  $7.4 \pm 2.5 \times 10^{-4} \text{s}^{-1}$  within a circular aperture of  $45''$  radius. The counts still increase somewhat at larger radii but the measurement is much noisier given the uncertainty in the sky determination. The total flux is thus approximately 10-30% larger than the above value. We convert the count-rate into a flux assuming an incident spectrum of  $T = 3$  keV and a local hydrogen column density of  $N_H = 2.61 \times 10^{21} \text{cm}^{-2}$ . The resulting unabsorbed flux is  $3.4 \pm 1.2 \times 10^{-14} \text{erg cm}^{-2} \text{s}^{-1}$  in the 0.1-2.4 keV band. We have also fitted a standard beta profile (Cavaliere & Fusco-Fermiano 1978) to the azimuthally averaged radial profile. We obtain best values for the core radius and beta parameter (slope decline at large radii) of  $15''$  and 0.80, respectively, although these values are quite uncertain given the low total number of counts.

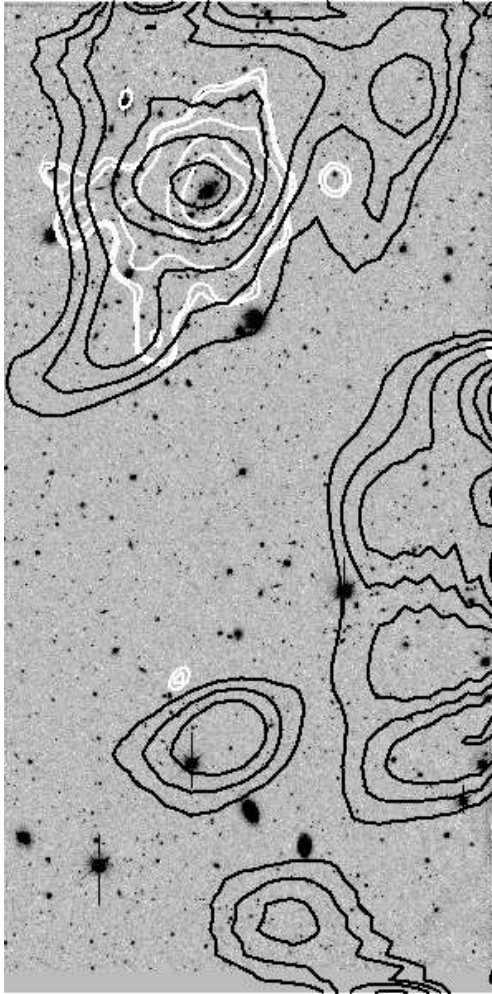


**Fig. 13.** For the UH8K-chip3 field, surface mass density (black) and X-ray (white) contours are plotted. The surface density contours are the same as in Fig. 5, whereas the X-ray contours correspond to  $1.5 \times 10^{-5}$ ,  $1.6 \times 10^{-5}$ ,  $2.0 \times 10^{-5}$ ,  $3.0 \times 10^{-5}$  and  $4.0 \times 10^{-5}$  counts/s/pixel. The cluster A1942 itself is clearly seen in X-rays, centered on the brightest cluster galaxy. In addition, extended X-ray emission near the dark clump is detected.

The X-ray luminosity depends on the redshift of the source. Assuming an incident spectrum at the detector of  $T = 3$  keV [ $T = 3(1+z)$  keV at the source], the rest-frame X-ray luminosity in the 0.1–2.4 keV band would range from  $1.9 \pm 0.6 \times 10^{42} h^{-2}$  erg s $^{-1}$  if the redshift is the same as that of A1942 ( $z = 0.223$ ) to  $3.5 \pm 1.2 \times 10^{43} h^{-2}$  erg s $^{-1}$  if  $z = 1.0$  ( $q_o = 0.5$ ).

We have also made a crude estimate of the mass of the system. On the one hand, if we assume an X-ray luminosity–temperature relation (e.g. Reichart et al 1999, Arnaud & Evrard 1999) and a temperature–mass relation (e.g. Mohr et al 1999), we can get mass estimates at a  $0.5 h^{-1}$  Mpc radius from  $1.5 \times 10^{13} h^{-1} M_{\odot}$  at  $z = 0.223$  to  $1.6 \times 10^{14} h^{-1} M_{\odot}$  at  $z = 1$  ( $q_o = 0.5$ ). We can also assume a beta profile, fixing the core radius and the beta parameter, and compute the normalization necessary to obtain the observed flux at the measured radius. Then we can integrate the profile to obtain the gas mass. If we

further assume a gas fraction, we can also obtain a total mass estimate. If we take the values obtained from our previous fit of the X-ray surface brightness profile, we get total masses at a radius of  $0.5 h^{-1}$  Mpc, of  $9.2 \times 10^{12} h^{-1} M_{\odot}$  at  $z = 0.223$  and  $2.3 \times 10^{13} h^{-1} M_{\odot}$  at  $z = 1$  ( $q_o = 0.5$ ). Note the difference of a factor of 1.5 and 7 compared to the previous estimates. This gives an indication of the errors involved. If instead we were to use typical values of the core radius and beta parameter of most clusters of galaxies (e.g.  $r_c = 0.125 h^{-1}$  Mpc and  $\beta = 2/3$ ) the mass estimates would be approximately a factor 3 larger and closer to the estimates using standard correlations.

Although we have presented quantitative values for the mass of the system based on the X-ray data, these should be taken only as informative given the assumptions and errors involved. Our main point in presenting these estimates is to show that this system has the X-ray properties of a galaxy group if it is at the same redshift as A1942. The lensing shear signal measured would then be too large for such a group unless it had a remarkable unusually high mass-to-X-ray light ratio. It seems more plausible that the system is a more massive cluster of galaxies at a higher redshift if the X-ray and lensing signal do indeed come from the same source, although the X-ray derived mass is still lower than the one obtained from the shear signal. The small angular scale X-ray core radius (larger physical scale if at larger redshift) and the lack of bright galaxies also point towards the same conclusion.

As an alternative, as suggested by Fig. 11 is that the X-ray emission may be unrelated to the dark clump, since the X-ray center of emission is located at  $\sim 3 \sigma$  from the center of the dark clump. Indeed the X-ray emission could be associated with the small projected galaxy number overdensity nearby, as seen from the black contours in the right-hand panel of Fig. 5. In that case, both the local enhancement of the galaxy density and the X-ray emission may be compatible with a group of galaxies, rather than a massive cluster, as indicated by the weak lensing analysis.

#### 4. Discussion and conclusions

Using weak lensing analysis on a deep high-quality wide-field  $V$ -band image centered on the cluster Abell 1942, we have detected a mass concentration some  $7'$  South of the cluster. This detection was confirmed by a deep  $I$ -band image. No clear overdensity of bright galaxies spatially associated with this mass concentration is seen; therefore, we termed it the ‘dark clump’. A slight overdensity of galaxies is seen  $\sim 1'$  ( $\sim 3 \sigma$ ) away from the mass center of the dark clump, but it is unclear at present whether it is physically associated with the mass concentration. Archival X-ray data allowed us to detect a  $3.2\text{-}\sigma$  X-ray source near the dark clump, separated by 60 arcseconds from its peak; it appears to be extended. The X-ray source is spatially coincident with the slight galaxy overdensity.

We have estimated the significance of the detection of this mass peak, using the field and the peak statistics. For the  $V$ -band image, the probability that the observed value in the field is caused by random noise of the intrinsic galaxy ellipticities

is  $\sim 10^{-6}$ ; a similar estimate from the *I*-band image yields a probability of  $\sim 4 \times 10^{-4}$ . The peak statistic gives a probability of  $\sim 10^{-4}$  for the *V*-band, and  $\sim 5 \cdot 10^{-3}$  for the *I*-band. Thus, the mass peak is detected with extremely high statistical significance. A bootstrapping analysis has shown that the tangential image alignment is not dominated by a few galaxy images, as also confirmed by the smooth dependence of the tangential shear on the angular separation from its center. Whereas these statistical tests cannot exclude any systematic effect during observations, data reduction, and ellipticity determination, the fact that this dark clump is seen in two independent images, taken in different filters and with different cameras, make such systematics as the cause for the strong alignment highly unlikely. Although we have accounted for the slight anisotropy of the PSF, the uncorrected image ellipticities yield approximately the same result.

A simple mass estimate of the dark clump shows it to be truly massive, with the exact value depending strongly on its redshift and the redshift distribution of the faint background galaxies. The mass inside a sphere of radius  $0.5h^{-1}$  Mpc is  $\gtrsim 10^{14}h^{-1}M_{\odot}$ , if an isothermal sphere model is assumed; if the lens redshift is larger, this lower mass limit increases, by about a factor 2 for  $z \sim 0.5$  and a factor of about 10 for  $z \sim 1$ . In any case, this mass estimate appears to be incompatible with the X-ray flux if the dark clump corresponds to a ‘normal cluster’, at any redshift. We therefore conclude that the mass concentration, though of a mass that is characteristic of a massive cluster, is not a typical cluster. This conclusion is independent of whether the X-ray emission is physically associated with the dark clump or not.

The lack of an obvious concentration of galaxies near the mass peak has been transformed into an upper limits on the luminosity associated with the mass concentration, and therefore into a lower limit of the mass-to-light ratio. This  $M/L$  limit depends again strongly on the redshift distribution of the faint galaxies, as well as on the assumed clump redshift. Whereas values for  $M/L$  as low as  $\sim 200$  (in solar units) are theoretically possible if the clump has a redshift in excess of unity, the corresponding mass becomes excessively and unrealistically large; for more reasonable redshifts  $z_d \lesssim 0.8$ ,  $M/L \gtrsim 450$  for an Einstein-de Sitter Universe, and  $M/L \gtrsim 300$  for a low density flat Universe. We would like to point out, though, that estimates of the  $M/L$ -ratio quoted in the literature practically never assume a  $\Lambda$ -dominated cosmology, so that the  $M/L$  ratio quoted above for the low-density Universe cannot be directly compared to literature values. For an Einstein-de Sitter Universe our lower limit of  $M/L \sim 450$  is not unusual (see Mellier 1998 for a review) but we have to emphasize that this limit is highly conservative.

We can only speculate about the nature of this dark clump. As argued above, a normal cluster seems to be ruled out, owing to the lack of bright X-ray emission. Whereas the estimated X-ray luminosity can be increased by shifting the putative cluster to higher redshifts, the corresponding lens mass also increases with  $z_d$ , in a way which depends on the redshift distribution of the source galaxies. The spatial coincidence of the slight galaxy overdensity and the X-ray emission, both  $\sim 1'$  away from the

mass center of the dark clump, may best be interpreted as a galaxy group or weak cluster at relatively low redshift and not associated with the dark clump.

The dark clump itself may then be a mass concentration with either low baryon density or low temperature, or both. For example, it may correspond to a cluster in the process of formation where the gas has not yet been heated to the virial temperature so that the X-ray luminosity is much lower than expected for a relaxed cluster. The fact that the tangential shear decreases towards the center of the mass clump may indeed be an indication of a non-relaxed halo.

Further observations may elucidate the nature of this mass concentration. Deep infrared images of this region will allow us to check whether an overdensity of IR-selected galaxies can be detected, as would be expected for a high-redshift cluster, together with an early-type sequence in the color-magnitude diagram. A deep image with the Hubble Space Telescope would yield a higher-resolution mass map of the dark clump, owing to the large number density of galaxies for which a shape can be measured, and thus determine its radial profile with better accuracy. Images in additional (optical and IR) wavebands can be used to estimate photometric redshifts for the background galaxies. In conjunction with an HST image, one might obtain ‘tomographic’ information, i.e., measuring the lens strength as a function of background source redshift; this would then yield an estimate of the lens redshift. The upcoming X-ray missions will be considerably more sensitive than the ROSAT HRI and will therefore be able to study the nature of the X-ray source in much more detail. And finally, one could seek a Sunyaev-Zel’dovich signature towards the dark clump; its redshift-independence may be ideal to verify the nature of a high-redshift mass concentration.

But whatever the interpretation at this point, one must bear in mind that weak lensing opens up a new channel for the detection of massive halos in the Universe, so that one should perhaps not be surprised to find a new class of objects, or members of a class of objects with unusual properties. The potential consequences of the existence of such highly underluminous objects may be far reaching: if, besides the known optical and X-ray luminous clusters, a population of far less luminous dark matter halos exist, the normalization of the power spectrum may need to be revised, and the estimate of the mean mass density of the Universe from its luminosity density and an average mass-to-light ratio may change. We also remind the reader that already for one cluster, MS1224, an apparently very high mass-to-light ratio has been inferred by two completely independent studies (Fahlman et al. 1994; Fischer 1999).

*Acknowledgements.* We thank Emmanuel Bertin, Stephane Charlot, Nick Kaiser, Lindsay King, Simon White and the referee for useful discussions and suggestions. We are grateful to Stephane Charlot for providing the *K*-corrections of elliptical galaxies in the *I*-band. We thank the Terapix data center (<http://terapix.iap.fr/>) for computing facilities. This work was supported by the TMR Network ‘‘Gravitational Lensing: New Constraints on Cosmology and the Distribution of Dark Matter’’ of the EC under contract No. ERBFMRX-CT97-0172, the ‘‘Sonder-

forschungsbereich 375-95 für Astro-Teilchenphysik” der Deutschen Forschungsgemeinschaft, and a PROCOPE grant No. 9723878 by the DAAD and the A.P.A.P.E.

## References

- Arnaud M., Evrard A.E., 1999, MNRAS 305, 631  
 Athreya R., Mellier Y., Van Waerbeke L., et al., 2000, A&A submitted (astro-ph/9909518)  
 Bahcall N.A., Fan X., 1998, ApJ 504, 1  
 Bartelmann M., Narayan R., Seitz S., Schneider P., 1996, ApJ 464, L115  
 Baugh C.M., Cole S., Frenk C. S., 1996, MNRAS 282, L27  
 Bertin E., Arnouts S., 1996, A&A 117, 393  
 Bond J.R., Efstathiou G., 1987, MNRAS 226, 655  
 Borgani S., Plionis M., Kolokotronis V., 1999, MNRAS 305, 866  
 Bruzual G.A., Charlot S., 1993, ApJ 405, 538  
 Cavaliere A., Fusco-Fermiano R., 1978, A&A 70, 677  
 Cuillandre J.C., Mellier Y., Dupin J.-P., et al., 1997, PASP 108, 1120  
 Eke V.R., Cole S., Frenk C.S., 1996, MNRAS 282, 263  
 Fahlman G., Kaiser N., Squires G., Woods D., 1994, ApJ 437, 56  
 Fischer P., 1999, astro-ph/9901407  
 Hoekstra H., Franx M., Kuijken K., Squires G., 1998, ApJ 504, 636 (HFKS98)  
 Jain B., Seljak U., White S.D.M., 1999, In: Banday A.J., Sheth R.K., Da Costa L.N. (eds.) Proceedings of the MPA/ESO Conference: Evolution of Large Scale Structures: From Recombination to Garching. PrintPartners Ipskamp  
 Jenkins A., Frenk C.S., Pearce F.R., et al., 1998, ApJ 499, 20  
 Kaiser N., Squires G., Fahlmann G.G., Woods D., 1994, In: Durret F., Mazure A., Tran Thanh Van J. (eds.) Clusters of Galaxies. Proceedings of the XXIXth Rencontre de Moriond  
 Kaiser N., Squires G., Broadhurst T., 1995, ApJ 449, 460 (KSB95)  
 Kruse G., Schneider P., 1999, MNRAS 302, 821  
 Lacey C., Cole S., 1993, MNRAS 262, 627  
 Landolt A. U., 1992, AJ 104, 340  
 Lilly S.J., Tresse L., Hammer F., Crampton D., Lefevre O., 1995, ApJ 455, 108  
 Luppino G.A., Kaiser N., 1997, ApJ 475, 20  
 Luppino G.A., Bredthauer R., Geary J. C., 1994, SPIE 2198, 810  
 Mellier Y., 1998, ARA&A 37, 127  
 Mohr J.J., Mathiesen B., Evrard A.E., 1999, ApJ 517, 627  
 Navarro J., Frenk C.S., White S.D.M., 1997, ApJ 490, 493  
 Press W.H., Schechter P., 1974, ApJ 187, 425  
 Reblinsky K., Kruse G., Jain B., Schneider P., 1999, A&A, in press  
 Reichart D.E., Castander F.J., Nichol R.C., 1999, ApJ 516, 1  
 Richstone D., Loeb A., Turner E.L., 1992, ApJ 393, 477  
 Schneider P., 1996, MNRAS 283, 837  
 Schneider P., Seitz C., 1995, A&A 294, 411  
 Schneider P., Van Waerbeke L., Jain B., Kruse G., 1998, MNRAS 296, 873  
 Seitz S., Schneider P., 2000, A&A submitted (astro-ph/9802051)  
 Snowden S., Kuntz K.D., 1998, ESAS documentation, <ftp://legacy.gsfc.nasa.gov/rosat/software/fortran/esas>.  
 Snowden S.L., McCammon D., Burrows D.N., Mendenhall J.A., 1994, ApJ 424, 714  
 van Waerbeke L., 1999, MNRAS accepted